AIAA SciTech
4-8 January 2016, San Diego, California, USA
54th AIAA Aerospace Sciences Meeting

Computational Analysis, Model Reduction, and Experimental Comparison of Model Scale Impinging Jets

Andrew R. Crowell, PhD[1]
NAVAIR, Patuxent River, MD, 20670

Leighton M. Myers[2]
The Pennsylvania State University, PA, 16802

Abstract

Computational fluid dynamics models and corresponding reduced-order models are compared with the results of a recent set of experiments on dual model scale impinging jets conducted at the Pennsylvania State University high speed jet aeroacoustics facility. Two studies are conducted comparing CFD and experiment: (1) supersonic jet plume analysis and (2) comparison of the pressure distributions on the underside of a lift plate as a function of nozzle pressure ratio and height above the ground. Results generally show good agreement between CFD and the experiment. However, there is clear room for improvement with CFD, specifically related to over predicting the strength of the pressure differential due to fountain flow impingement on the underside of the lift plate. Additionally, reduced-order modeling techniques are applied to CFD solutions in order to conduct a large scale parametric study. This study revealed the effect various parameters have on specific outputs of interest, including: suckdown force, peak heat flux, outwash velocity, and several others. A computational cost analysis demonstrates the parametric study would have been impractical without the reduced-order modeling effort.

Nomenclature

A^*	=	area of the throat of the nozzle
D	=	diameter of nozzle exit
H	=	height above the ground plane
K	=	number of sample points for ROM evaluation
$\dot{m}$	=	mass flow
n	=	number of sample points for ROM generation
NPR	=	nozzle pressure ratio
P	=	pressure
Q_{aero}	=	aerodynamic heat flux
R	=	gas constant
T	=	temperature
TTR	=	total temperature ratio
U	=	headwind velocity
V	=	velocity
γ	=	ratio of specific heats, 1.4

Subscripts

$_0$	=	stagnation
$_\infty$	=	free stream
$_e$	=	exit
$_{FJ}$	=	front jet
$_{RJ}$	=	rear jet

I. Introduction

Short take-off and vertical landing (STOVL) aircraft present numerous complications when in ground effect due to the impingement of hot, high speed jets on the ground or deck of a ship. These adverse effects depend on a

[1] Aerospace Engineer, Applied Aerodynamics and Store Separation Branch, AIAA Member.
[2] SMART Scholar, Aerospace Engineering, 229 Hammond Bldg., AIAA Student Member.

number of parameters, such as: height the jet is above ground[1], nozzle pressure ratio[1], total temperature ratio[2], initial turbulence of the jet[3], any shock cells that exist in the supersonic exhaust[3], and resonance conditions[3]. The jet impingement effects include: lift loss or "suckdown", aircraft/ground/deck erosion[4,5] due to high shear stress and high heat transfer rates from jet impingement on the ground and possible fountain flow impingement on the underside of the aircraft, large hazardous zones for the surrounding personnel/aircraft/structures due to the high velocity/pressure/temperature outwash, and hot gas ingestion where the outwash is drawn back into the engine degrading engine performance. One specific focus of research has been suckdown[1-4], which is caused by the exhaust of the jet(s) physically entraining the flow due to the action of the shear layer and the surrounding air. Krothapalli *et al*[1] reported suckdown forces as high as 60% of the ideal thrust for a single downward jet, when the jet is within two nozzle exit diameters of the ground. Kumar *et al*[2] performed a similar experiment in the same facility with a heated jet (nozzle exit temperature 480 K). They observed that not only are the pressure fluctuations generated by hot impinging jets much higher than those due to cold jets, the hover suckdown force is also much higher. For comparable heights above the ground plane, the hover suckdown force for the heated jet is 75% of primary jet thrust.

Some of the jet impingement effects are best illustrated in an actual STOVL flight environment. Specifically, after 14 sequential take-offs of the Harrier aircraft, the deck of the LPH Tripoli buckled, forming an 8 inch deep depression which required over 16 hours to cool[5]. More recently, field-tests were performed by the U.S. Navy to measure the force exerted on the human body when standing beneath a hovering CH-47 rotorcraft[6]. While the disk loading of the tandem CH-47 is around 10 lbs/ft^2, that of a typical STOVL aircraft[7] such as the Harrier or F-35B Joint Strike Fighter (JSF) is around 1000 lbs/ft^2. Defining safe-operating zones around these hovering aircraft is paramount for the safety of those working in confined spaces aboard Navy carriers or amphibious assault ships. During initial sea trials in 2011, the F-35B performed its first vertical landing aboard a U.S. Navy L-class amphibious ship. Obtaining useful measurements at full scale in the field was very challenging due to high temperatures, flow-field unsteadiness, and acoustic pressures. McCarthy[8] reported on the difficulty of engineering the proper instrumentation and hardware support structure for static JSF nozzle plume studies.

Combining the complex flow-field of a hovering STOVL aircraft with the maritime environment makes full scale experimental testing especially challenging. Consequently, model scale impinging jets have presented a practical means of studying the fundamental physics, and have been a focus of research for over four decades[9]. A few notable experimental studies include the works of Krothapalli *et al*[2,10] and Kumar *et al*[3], which were mentioned previously; as well as Saddington *et al*[11], who considered the effect splayed jets have on vertical landing and fountain flow; and the works of Myers *et al*[12], who studied dual model scale jets, which will be further investigated in this paper. Additionally, Alvi *et al*[4], noted that it is possible to gain further insight into the complex physics involved in jet impingement through computational modeling, and used Computational Fluid Dynamics (CFD) Reynolds-averaged Navier-Stokes (RANS) models to repeat the experimental investigations of Krothapalli *et al*[2,10]. Several others have followed this computational approach, including the use of Large Eddy Simulation (LES)[13,14] and Delayed Detached Eddy Simulation (DDES)[15,16].

In this paper, the experimental model of Myers *et al*[12] will be investigated computationally using both RANS and DDES models. In order to gain a further perspective on the impact several parameters have on the adverse jet impingement effects, a simple reduced-order model (ROM) based on CFD will be developed. The ROM will enable an efficient and accurate parametric sweep of the identified parameter space and thus provide insight on how certain parameters affect specific outputs. The ROM will be constructed in the same manner as that described by Crowell and McNamara[17].

II. Experimental and Computational Models

A. Experimental Facility and Instrumentation Descriptions

The experiments presented in this paper were conducted in the Pennsylvania State University high-speed Jet Aeroacoustics Facility. An exhaust fan, installed in the downstream section of a collector, captures the jet exhaust and minimizes air recirculation. The open jet wind tunnel test section entrance has a cross section of approximately 60 cm x 60 cm, and is installed upstream of the dual impinging jets to provide the head-wind simulation as shown in Figure 1. The dual impinging jet nozzles include a convergent contoured nozzle (front sonic jet) and a converging-diverging (CD) contoured nozzle (rear supersonic jet). The convergent nozzle exit diameter (D_{FJ}) is 17.8 mm while the CD nozzle exit diameter (D_{RJ}) is 18.0 mm. The rear CD nozzle has a design Mach number of 1.65 (NPR_{RJ} = 4.58) and features twelve facets that extend through the divergent section to the exit. The faceted design of the throat and divergent sections was originally provided to Penn State by General Electric, GE, through a contract for the Strategic Environmental Research and Development Program. The faceted nozzle resembles the design of the GE F141 line of engines. For the experimental measurements, both nozzles were operated over a range of nozzle pressure ratios, which is defined as the ratio of total jet pressure in the plenum to static pressure at the nozzle exit. The static pressure at the exit was assumed equal to room ambient pressure which was recorded at the start of each run and typically maintained a value of 97.9 +/- 0.07 kPa. Additional measurements were obtained while simulating a heated exhaust from the rear jet using helium; however this paper only presents experimental results for the jets operating with a total temperature ratio (TTR) equal to 1.0 using standard air. The distance between the centerlines of the two nozzles is 10.6 D_{RJ} and the vertical distance between the exits of the two nozzles is 1 D_{RJ}. See Figure 2 for schematic diagrams of the dual impinging jet model. An aluminum ground plane, with a smooth machined surface, of dimensions 91.4 cm x 91.4 cm x 4.8 mm was used during the experiments. In general, the distance from the ground plane to the convergent nozzle exit was adjusted from 2 to 24 D_{RJ}. A rectangular aluminum sheet of dimensions 22.3 cm x 48.8 cm x 6.4 mm was used to represent a generic aircraft surface (lift plate). The lift plate was installed such that the exit of the convergent nozzle was flush with the lower surface of the plate. The converging-diverging nozzle penetrates the lower surface of the lift plate by 1 D_{RJ}. Further information on the experimental facility, nozzles, lift plate, and setup are detailed in Ref. 18.

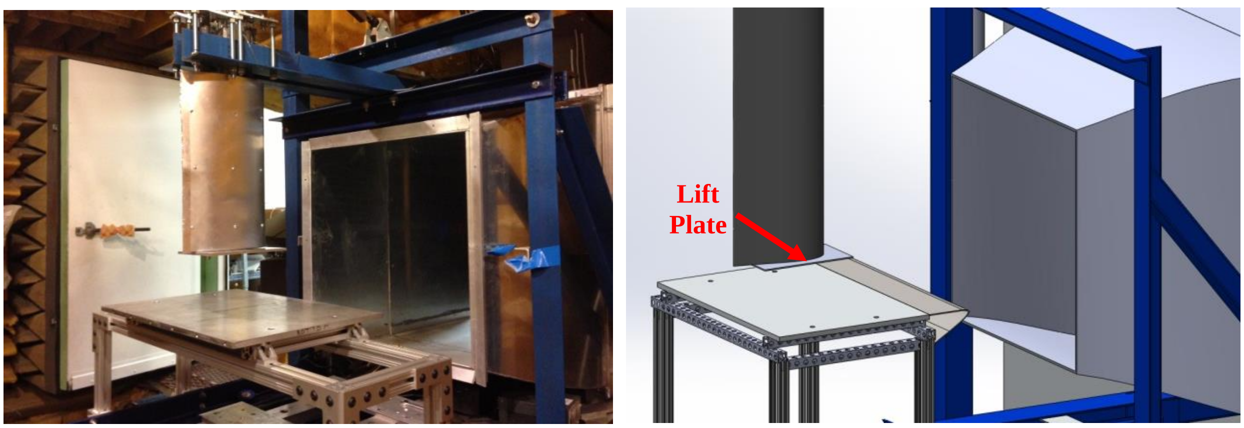

a) Photograph of the installed experiment setup. b) Schematic of the experiment setup.

Figure 1: Photograph and schematic of the experimental setup.

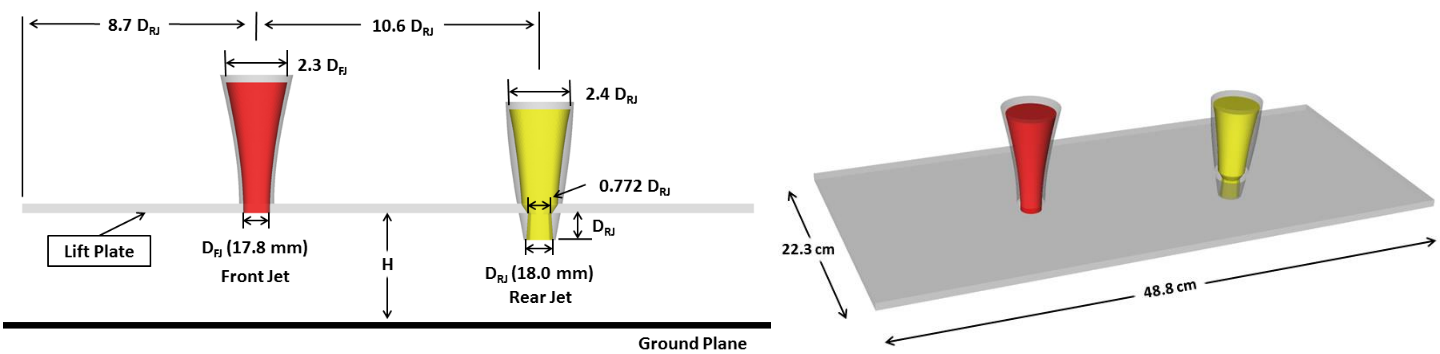

a) Dual jet model dimensions. b) Lift plate dimensions.

Figure 2: Schematic diagram of lift plate.

B. Computational Fluid Dynamics Model

The commercial CFD flow solver COBALT[19] was used for all CFD analyses. COBALT is an unstructured, Navier-Stokes solver with RANS and DDES capabilities. The code has second-order accuracy in both time and space. Several turbulence models are investigated, including: the Spalart-Allmaras (SA) model[20], the Menter shear stress transport (SST) model[21], the DDES model based on SA[22], and the DDES model based on SST[23]. Four grids were generated specifically to compare to the experimental results, and an additional 160 grids were generated for the parametric reduced-order modeling study. The surface and boundary layer cells are similar in all of the grids, only the distance between the ground and lift plate varies. The surface grids were generated using VGRID[24] and the volume grids were generated using AFLR3[25]. A boundary layer, time step, iteration, and sub-iteration convergence study was conducted using the most adverse conditions tested in the experiment; placing the dual jet model closest to the ground and at the highest rear jet nozzle pressure tested. From this study, the final CFD solution parameters and grid details were selected and are provided in Table 1. Representative images of the grids are provided in Figure 3. A sample CFD solution which illustrates the jet impingement regions on the ground plane and on the lift plate from the fountain flow is shown in Figure 4.

Table 1. CFD grid and solution parameters.

Parameter	Value
Ambient Conditions	Sea Level
Start-up Time Step	$2.5e^{-3}$ (s)
Start-up Iterations	2000
Final Time Step	$2.5e^{-5}$ (s)
Final Iterations	7500
Sub-iterations	5
Time Averaging Start	Iteration 4000
y^+	< 1
Surface Cells	300,000
Boundary Layer Cells	2.5 million
Total Number of Cells	12 to 16 million

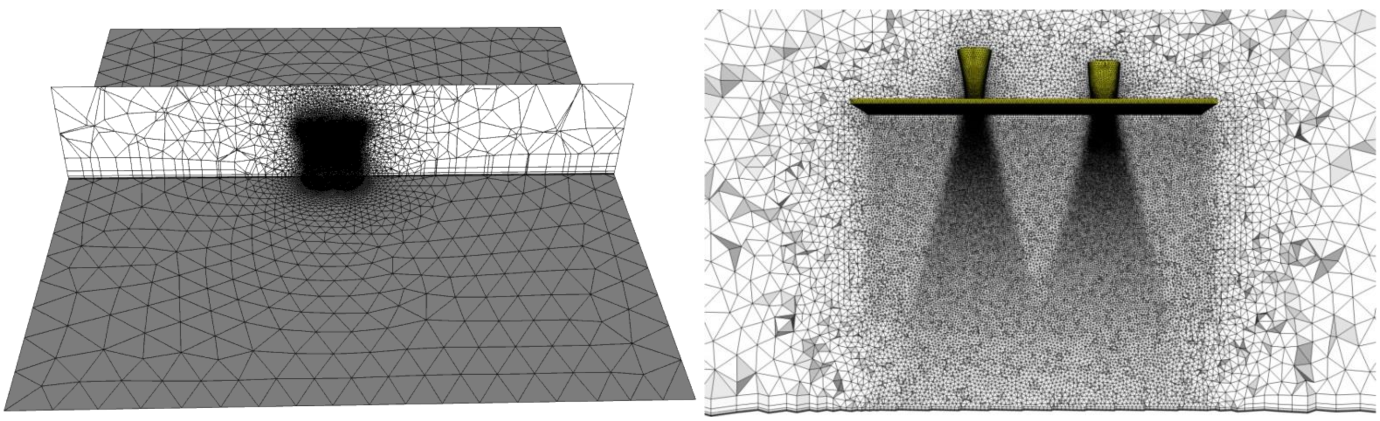

(a) Example CFD grid. (b) Cut plane veiw of the dual jet CFD model.

Figure 3: Dual jet CFD grid.

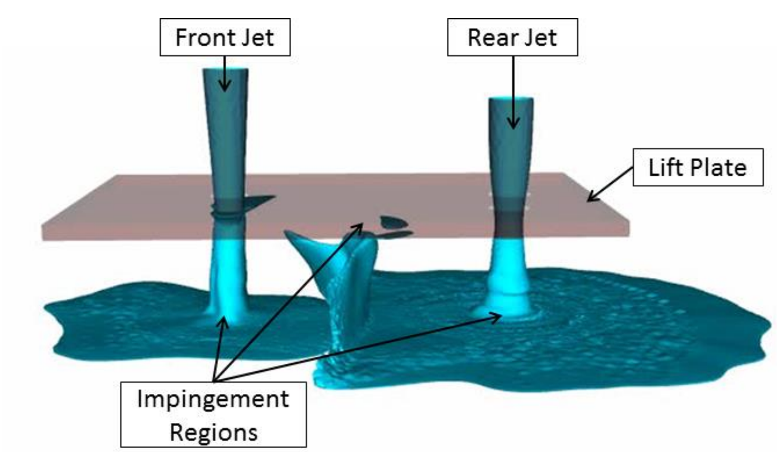

Figure 4. Sample CFD solution showing impingement regions and fountain flow.

C. CFD Reduced-Order Model

In order to gain a better understanding of how certain parameters alter jet impingement effects, such as suckdown or the outwash velocity/pressure/temperature, a parametric study is conducted with the use of reduced-order models (ROMs). The ROMs will be constructed in the same manner as that described by Crowell and McNamara[17]. A flowchart of the process to build the ROMs using time-averaged CFD data is provided in Figure 5. First, the input parameters and bounds for the model are established. These parameters and bounds provide the limits of the parametric study. Latin hypercube sampling is used to identify a diverse set of sampling points inside of this parameter space. Next $n + K$ training snapshots of the CFD response are computed from solutions to the Navier-Stokes equations at each of the sample points; n snapshots form the database for model construction and K snapshots are for evaluating the accuracy of the model. The actual ROM is computed using the n snapshot database and the Matlab® Design and Analysis of Computer Experiments[26] (DACE) kriging toolbox. This toolbox offers a number of methods for creating kriging interpolation models. Each of the available options in the toolbox is used, thus creating a number of models from the same database. The accuracy of each model is tested against the K snapshots and the most accurate model is saved. If further accuracy is desired, more sample responses are added to the database and the process is repeated. Note that a preferred approach for selecting the sampling points for the database would be an adaptive sampling procedure, where an initial set of sampling points is used to construct a baseline model, and subsequent points are selected systematically so as to efficiently sample the parameter space. Such a technique is often used in the optimization community[27]. However, the challenge in the context of this work is that a globally accurate model over the parameter space is sought, since a full parametric study is to be conducted. Existing adaptive sampling procedures are intended for the identification of an optimum configuration; thus, they are not applicable to this study. Thus while an important area of need, the development of such a procedure is left for future work. Further information on the construction of DACE kriging ROMs is detailed in previous work[17].

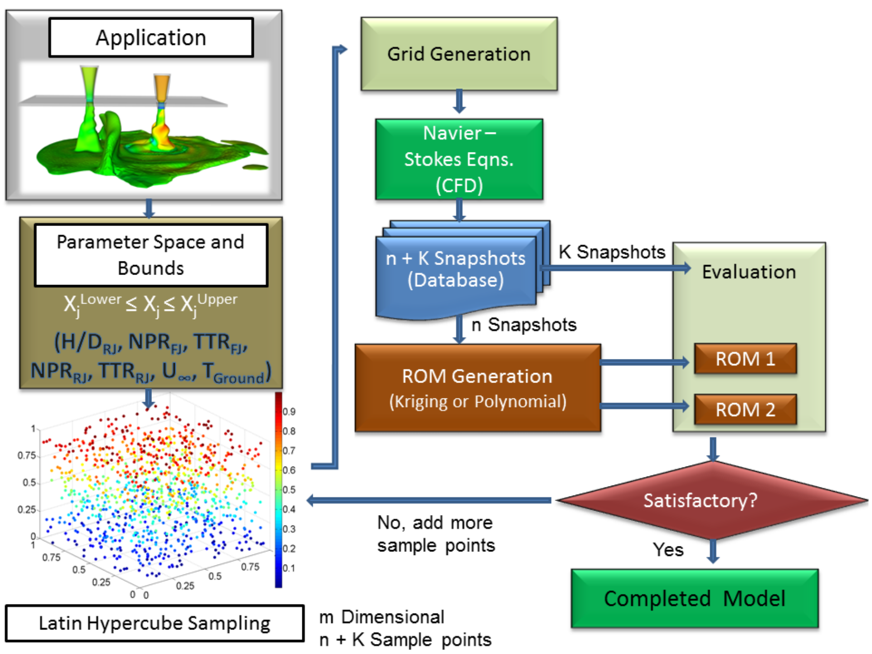

Figure 5: Reduced-order modeling framework.

III. Results and Discussion

A. Full-Order Computational Fluid Dynamics Results

In order to determine which turbulence model is best suited for this study, a plume survey was conducted for only the rear jet without the ground plane. The first set of results compare full-order CFD to the experiment for this setup. In the experiment, a five probe pitot rake was traversed through the plume and data was acquired at the locations shown in Figure 6a. In the first three diameters below the nozzle exit, data was collected in a very dense pattern. From three to eleven diameters below the nozzle exit, the pitot rake was traversed axially in increments of 0.5 D_{RJ}. The rake has a total aperture of 8.4 mm or about 0.5 D_{RJ}. The diameter of each individual probe that makes up the rake is equal to 0.06 D_{RJ}. The probe was allowed to rest at each survey location for a period of 50 ms before acquiring data. Data was collected using a rear nozzle pressure ratio of 2.927, a total temperature ratio of 1.0, and ambient sea level conditions.

CFD solutions were computed using the four different turbulence models mentioned in Section IIB, and the time-averaged total pressure data was extracted at the same tap locations as the experiment. A comparison down the centerline of the plume of the normalized total pressure (measured total pressure divided by the plenum total pressure) is shown in Figure 6b. Close to the nozzle exit, between z/D_{RJ} of 0 and -4, all four of the CFD models over predict the total pressure relative to the experiment. There may be several reasons for the discrepancy: (1) simple computational error, (2) experimental error resulting from placing the pitot rake in the flow-field, or (3) accounting for the bow shock in front of each probe in the rake using the Rayleigh pitot formula; where the formula assumes that the static pressure just upstream of the shock is equal to ambient pressure, which is not true when the nozzle is operating at off design conditions. Further from the nozzle exit, the SA and SST turbulence models show similar behavior to the experiment, while both the DDES models do not. The SA model has the best comparison from z/D_{RJ} of -4 to -8, and the SST model has the best comparison from -8 on.

Figure 7 shows the plume survey for each of the CFD turbulence models compared to experiment. The SA and SST models again compare favorably with the experiment, while the DDES models do not. The DDES models predict the core of the plume to extend beyond the measured tap locations with very little dissipation. In order to gain further insight into the spreading of the plume, the pitot rake was moved in planes perpendicular to the plume at 7 different locations below the nozzle exit. These results are shown in Figures 8 and 9. Figure 8 shows all of the data for both the experiment and the 4 CFD models, and Figure 9 shows only the centerline data ($y/D_{RJ} = 0$). From these figures several observations can be drawn. First, the SA model under predicts the spreading of the plume and over predicts the dissipation of the core, seen clearly at $z/D_{RJ} = -6$ and -8 in Figure 9a. Second, the SST model under predicts the dissipation of the core, but predicts the spreading of the plume quite accurately, seen in Figure 9c. Finally, neither DDES model predicts the core strength or the spreading of the plume accurately. Based on these observations the remaining CFD results are computed using the SST turbulence model.

The next set of results include both the front and rear jets as well as the ground plane. The ground plane was tested at four different locations below the lift plate, $H/D_{RJ} = 2$, 3, 6, and 12. Additionally, three different rear jet nozzle pressure ratios were tested, $NPR_{RJ} = 1.89$, 2.927, and 4; for a total of 12 different test conditions. The front jet was held to a NPR_{FJ} of 1.89 and the TTR for both nozzles was set at 1.0. Pressure data was acquired at 35 tap locations on the underside of the lift plate, shown in Figure 10a. The number of tap locations was limited by the data acquisition system used in the experiment. The taps are down the center and to the left of the jets because it is assumed that the pressure distribution on the underside of the lift plate is symmetric. Figure 10b provides a sample comparison of the CFD data extracted at the tap locations and the actual CFD surface data. The conditions for the sample CFD solution are: $H/D_{RJ} = 3$ and $NPR_{RJ} = 2.927$. The CFD surface data clearly shows a high pressure gradient that extends to the edge of the lift plate which occurred due to the impingement of the fountain flow on the lift plate. However, due to the restricted number of pressure taps and their locations, the tap-based data does not show the entirety nor does it fully resolve the high pressure region. For the sake of consistency with the experiment, the remaining pressure contour comparisons will use only the CFD data extracted at the tap locations.

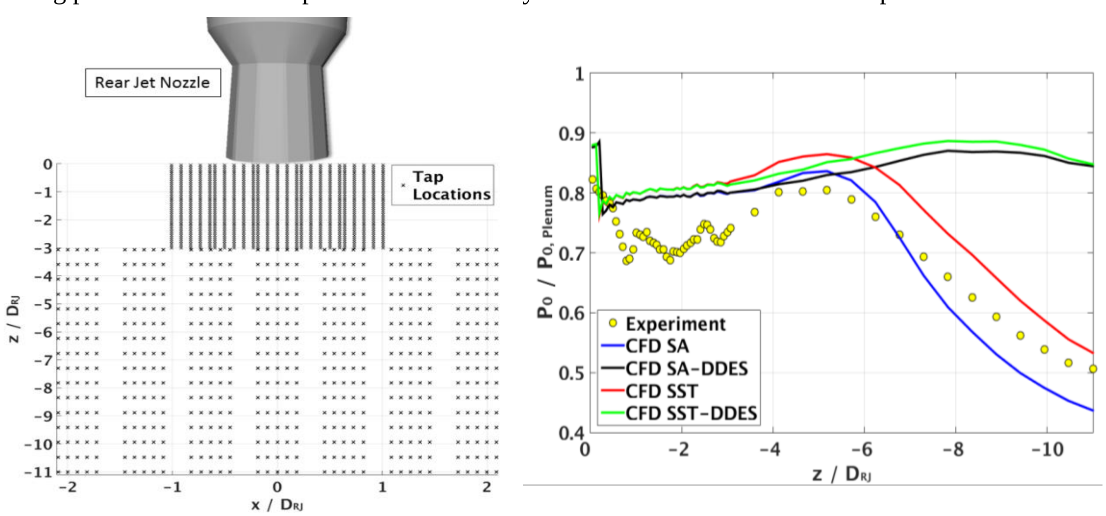

(a) Tap locations. (b) Centerline normalized pressure comparison.

Figure 6. Rear jet plume tap locations and centerline ($x / D_{RJ} = 0$) comparison with CFD.

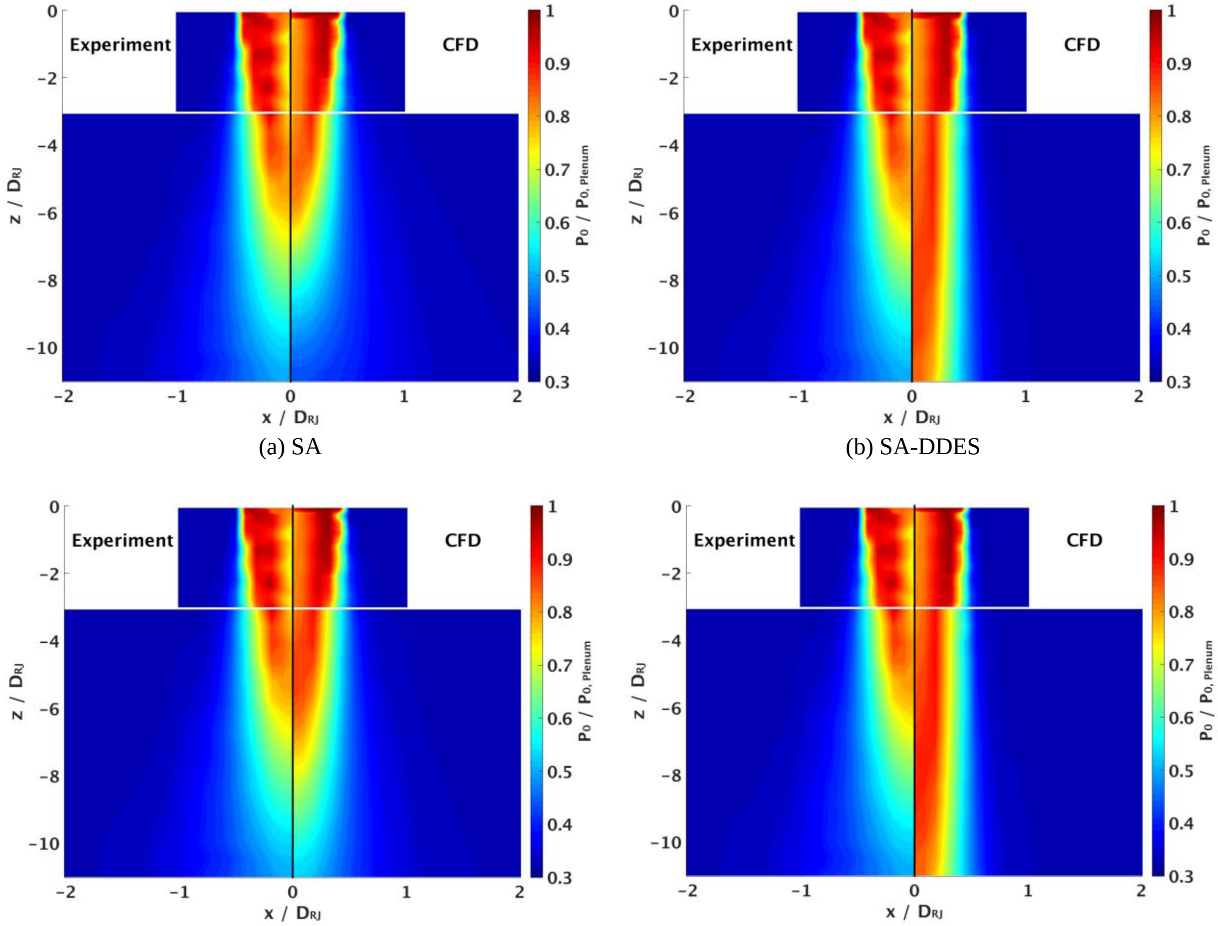

(a) SA (b) SA-DDES

(c) SST (d) SST-DDES

Figure 7. Rear jet experimental and CFD normalized pressure comparison, using cross-sections through the center of the plume. NPR_{RJ} = 2.927, TTR_{RJ} = 1.0, sea level ambient conditions.

Comparisons between experiment and CFD for the non-dimensional pressure differential down the center of the front and rear jets are presented in Figure 11. The non-dimensional pressure differential is computed as the difference between the pressure on the bottom of the lift plate and the ambient pressure divided by the total pressure of the rear jet. The rear jet nozzle pressure ratios considered are: (1) 1.89 in Fig. 11a, (2) 2.927 in Fig. 11b, and (3) 4.0 in Fig. 11c. Again, the lift plate is placed at four heights above the ground plane for each of the pressure ratios, H/D_{RJ} = 2, 3, 6, and 12. Only two of the four heights above the ground plane are presented for the lowest pressure ratio, due to both the poor comparison between CFD and the experiment for the other two conditions, as well as the additional data making trends difficult to identify. However, the excluded data in Figure 11a is included later, in Figure 12. For the two heights presented in Figure 11a, the CFD model fairly accurately predicts the location and magnitude of the high pressure gradient caused by the fountain flow impinging on the underside of the lift plate. In Figures 11b and 11c, the experiment and CFD are in good agreement except for the magnitude of the pressure differential at the impingement location for H/D_{RJ} = 2 and 3. Additionally, the CFD solutions show a slight increase in pressure at H/D_{RJ} = 6, while the experiment does not.

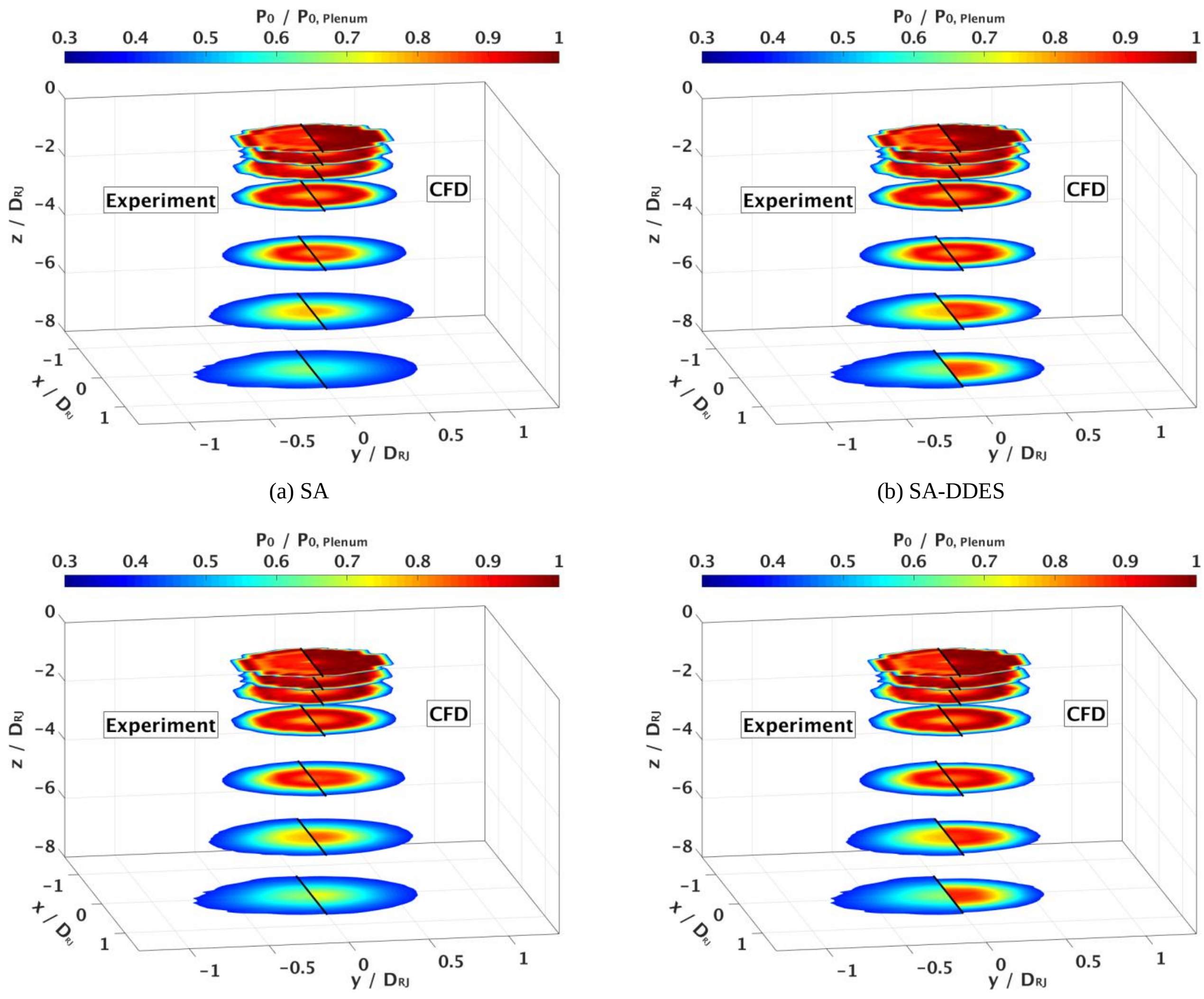

(a) SA

(b) SA-DDES

(c) SST

(d) SST-DDES

Figure 8. Rear jet experimental and CFD normalized pressure comparison, using cross-sections perpendicular to the plume. NPR_{RJ} = 2.927, TTR_{RJ} = 1.0, sea level ambient conditions.

The next set of results, presented in Figures 12, 13, and 14, show the non-dimensional pressure differentials for all of the tap locations for NPR_{RJ} = 1.89, 2.927, and 4.0, respectively. The comparison between the experiment and CFD for H/D_{RJ} = 2 at NPR_{RJ} = 1.89, Figure 12a, is somewhat poor. The CFD solution under predicts the magnitude and incorrectly predicts the location of the fountain flow impingement on the lift plate. In Figure 12b, H/D_{RJ} = 3, the magnitude and location of the peak pressure for CFD and the experiment compare well, however the overall distribution does not match. The best comparison for this NPR is at H/D_{RJ} = 6, Figure 12c, where both the magnitude and distribution of the pressure are very similar. At H/D_{RJ} = 12, Figure 12d, the CFD solution over predicts the pressure differential caused by the fountain flow impingement.

Figures 13 and 14 present the results for NPR_{RJ} = 2.927 and 4.0, respectively. For both of these rear jet pressure ratios at H/D_{RJ} = 2, 3, and 6 the CFD model correctly predicts the location of the fountain flow impingement, but over predicts the pressure differential at that location. At H/D_{RJ} = 12, neither the experiment or CFD show a pressure increase due to the fountain flow impingement and are therefore in agreement. Note though the magnitude of the pressure differentials in Figures 13 and 14 appear similar, due to the non-dimensionalization, the actual pressure acting on the lift plate for NPR_{RJ} = 4.0 is significantly higher.

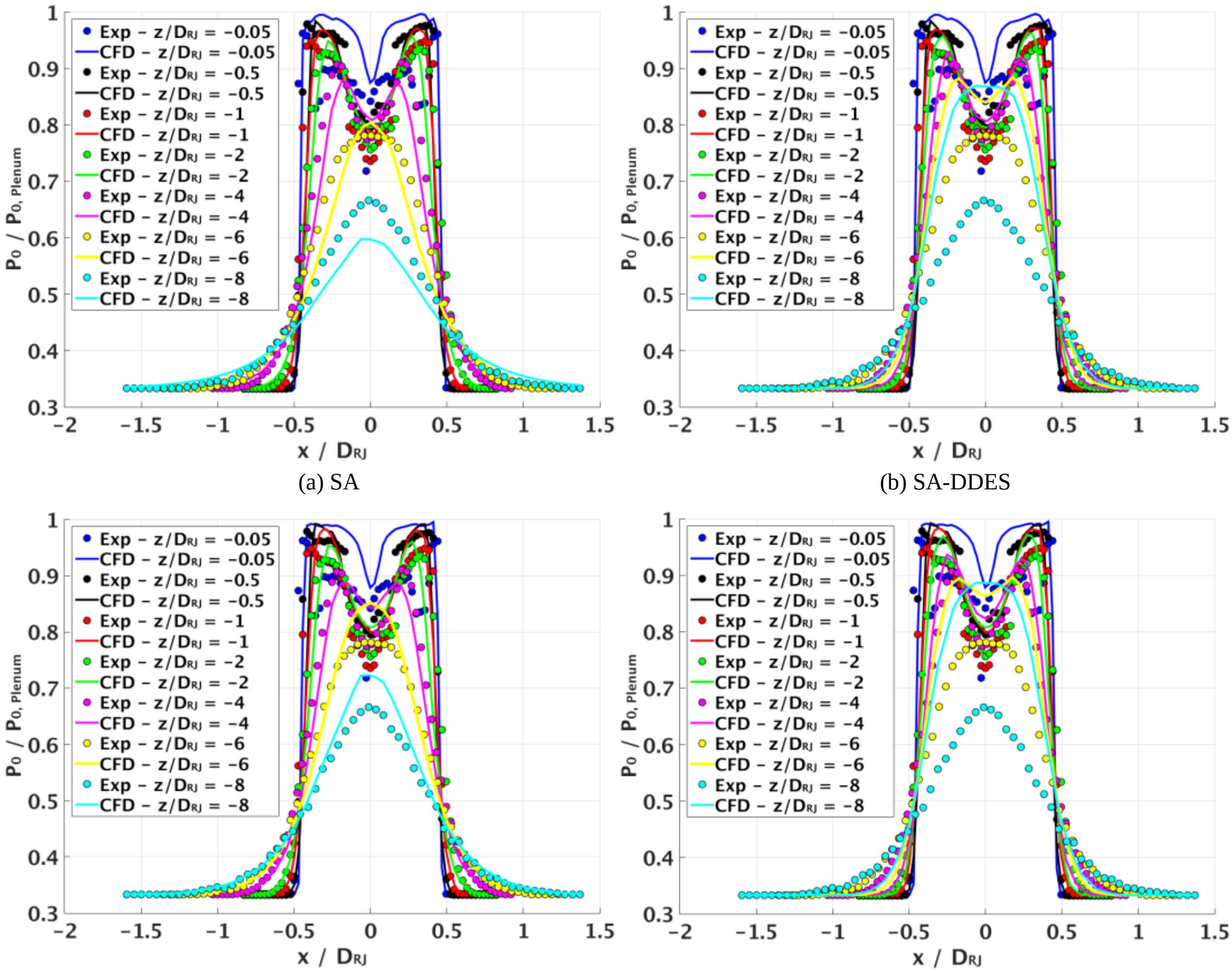

(a) SA (b) SA-DDES

(c) SST (d) SST-DDES

Figure 9. Rear jet experimental and CFD normalized pressure centerline comparisons at several z locations. NPR_{RJ} = 2.927, TTR_{RJ} = 1.0, sea level ambient conditions.

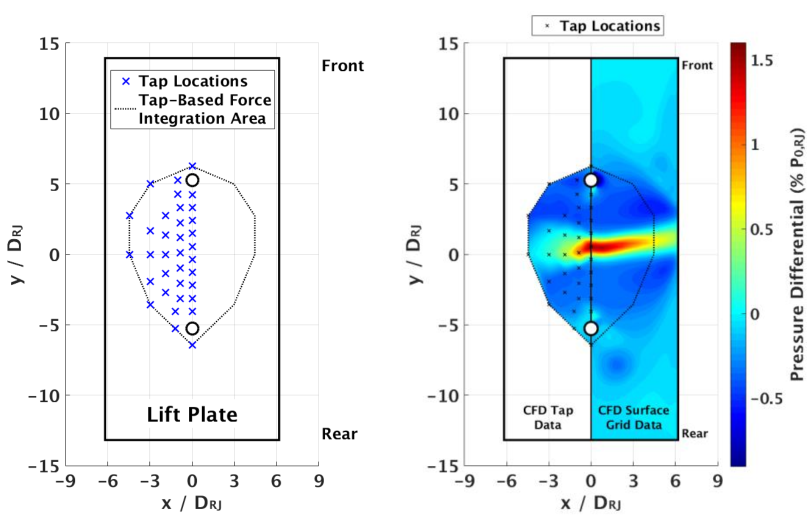

(a) Tap locations. (b) Example CFD tap data vs. CFD surface data.

Figure 10. Tap locations on the bottom of the lift plate. Circles indicate nozzle exit locations.

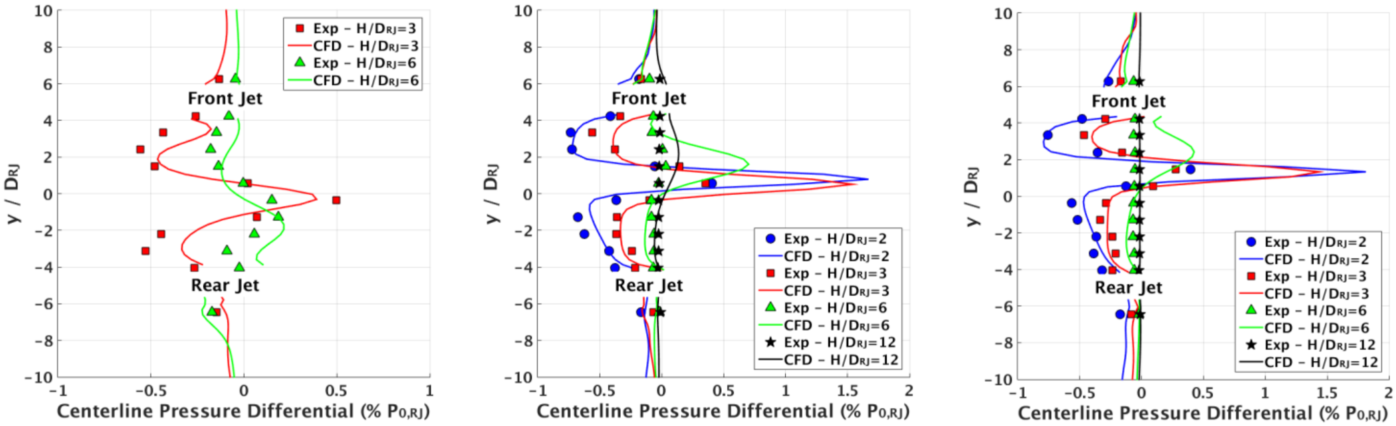

(a) $NPR_{RJ} = 1.89$. (b) $NPR_{RJ} = 2.927$. (c) $NPR_{RJ} = 4.0$.

Figure 11. Experimental and CFD non-dimensional pressure differential comparison of the lift plate centerline.

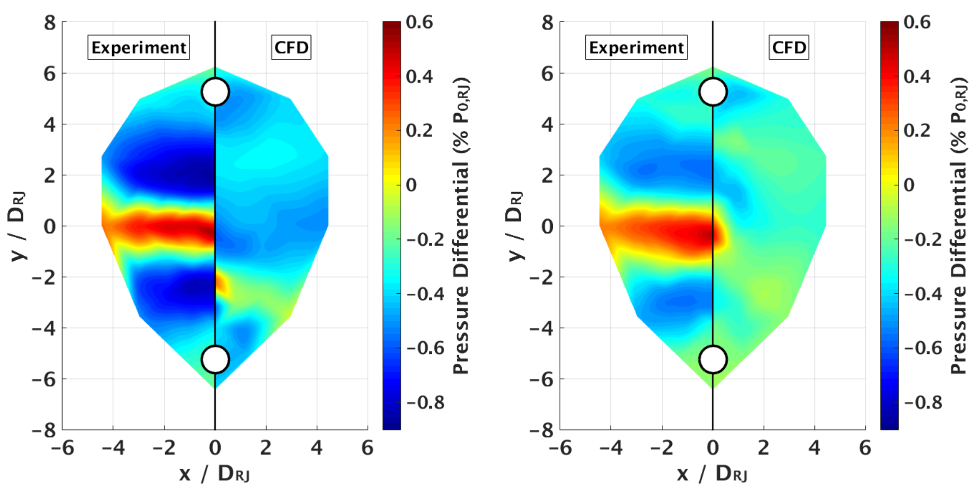

(a) $H / D_{RJ} = 2$ (b) $H / D_{RJ} = 3$

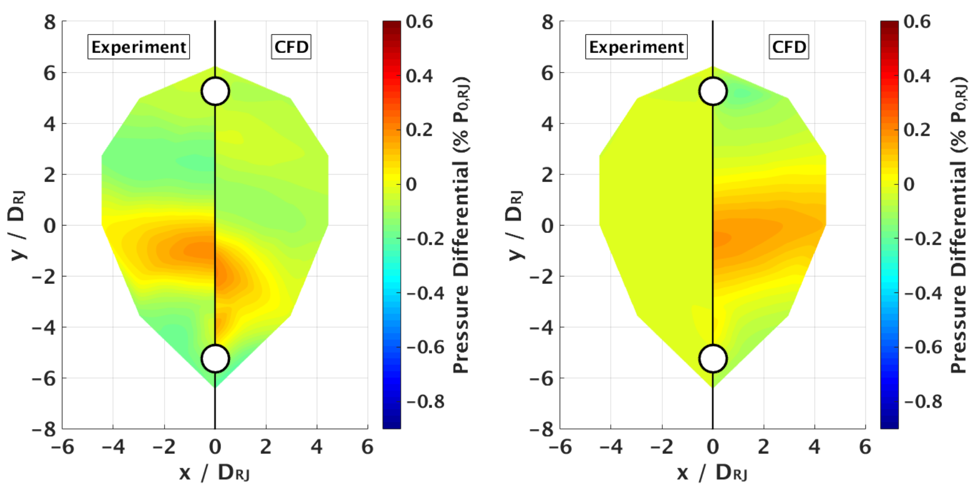

(c) $H / D_{RJ} = 6$ (d) $H / D_{RJ} = 12$

Figure 12. Experimental and CFD non-dimensional pressure differential comparisons on the bottom of the lift plate. $NPR_{RJ} = 1.89$.

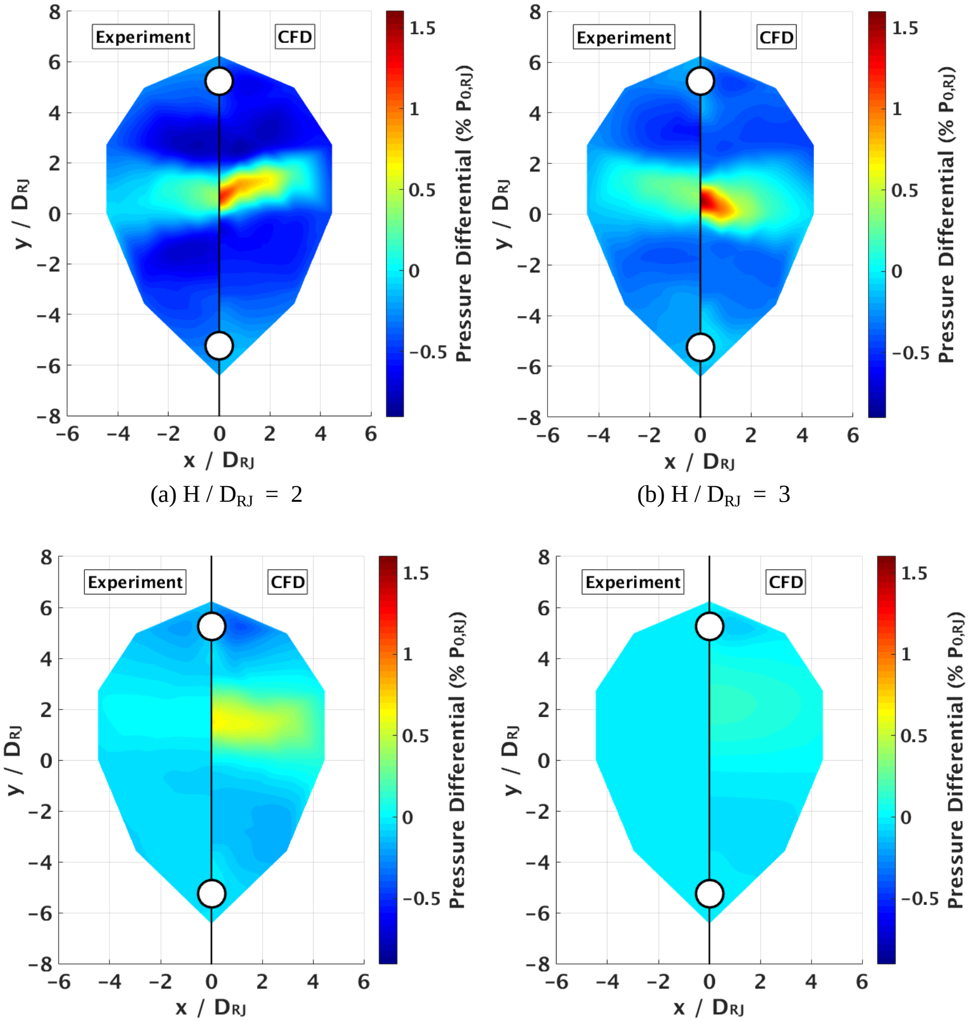

(a) H / D_{RJ} = 2 (b) H / D_{RJ} = 3

(c) H / D_{RJ} = 6 (d) H / D_{RJ} = 12

Figure 13. Experimental and CFD non-dimensional pressure differential comparisons on the bottom of the lift plate. NPR_{RJ} = 2.927.

The final comparison conducted between the experiment and CFD is for the computed suckdown force, presented in Figure 15. The tap-based force integration area is shown in Figure 10a, where the pressure differential on the underside of the lift plate is again assumed to be symmetric about the line down the center of the front and rear jets. In addition to presenting the experimental and CFD tap-based suckdown force, the suckdown force calculated using the entire lift plate surface pressure from CFD is also included. Note, the forces are normalized by the combined ideal thrust of the front and rear jets, using:

$$\dot{m} = A^* \frac{P_0}{\sqrt{T_0}} \sqrt{\frac{\gamma}{R}} \left(\frac{\gamma+1}{2}\right)^{\frac{-\gamma-1}{2\gamma-2}} \tag{1}$$

$$V_e = \sqrt{T_0 R \frac{2\gamma}{\gamma-1} \left(1 - \left(\frac{P_\infty}{P_0}\right)^{\frac{\gamma-1}{\gamma}}\right)} \tag{2}$$

$$\text{Ideal Thrust} = \dot{m}_{FJ} V_{e,FJ} + \dot{m}_{RJ} V_{e,RJ} \tag{3}$$

where $\dot{m}$ is the mass flow, A^* is the nozzle throat area, and V_e is the exit velocity.

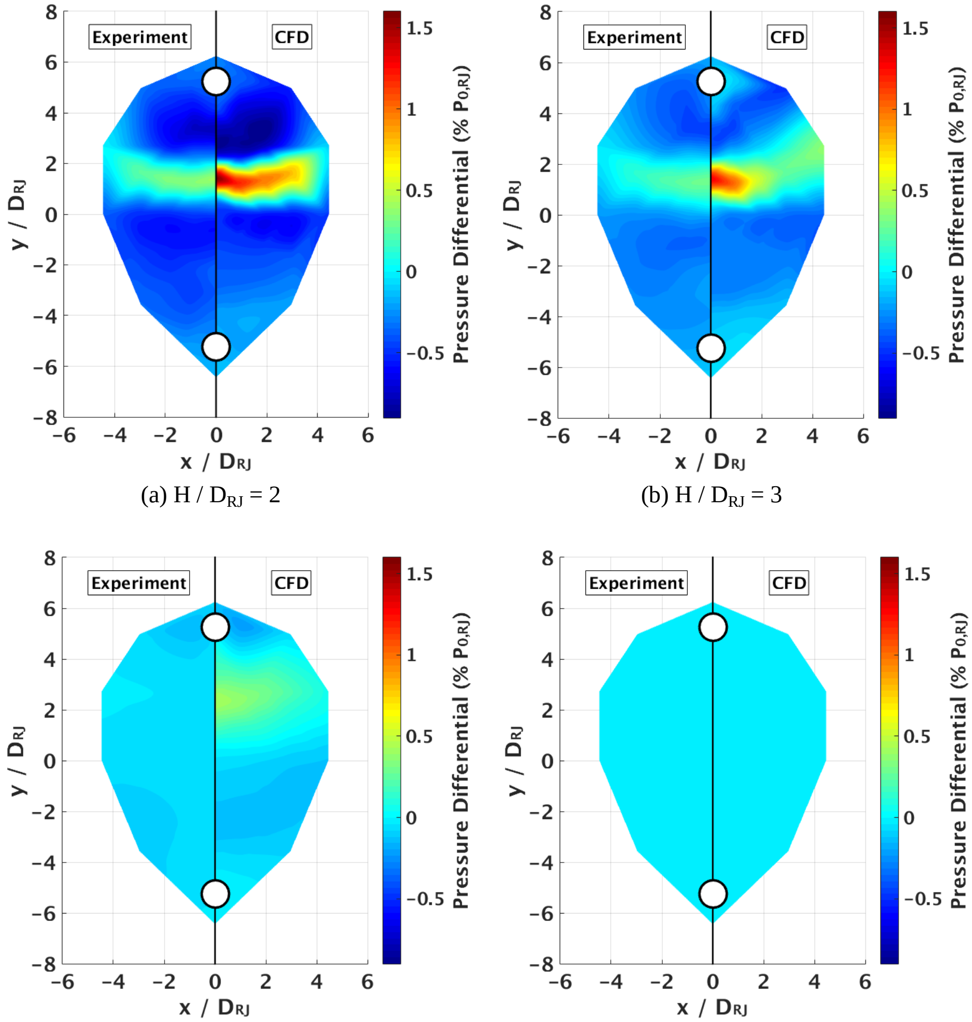

(a) $H / D_{RJ} = 2$ (b) $H / D_{RJ} = 3$ (c) $H / D_{RJ} = 6$ (d) $H / D_{RJ} = 12$

Figure 14. Experimental and CFD non-dimensional pressure differential comparisons on the bottom of the lift plate. NPR_{RJ} = 4.0.

Several observations can be made about the suckdown forces shown in Figure 15. First, by normalizing the suckdown force relative to the ideal thrust, the suckdown force roughly collapses for each of the nozzle pressure ratios considered. Second, as the lift plate gets closer to the ground the suckdown force becomes significantly stronger. Third, surprisingly the best comparison between CFD and the experiment for the tap-based force occurs at NPR_{RJ} = 1.89, even though the pressure contours appeared to be the most dissimilar in Figures 12-14. The worst agreement in Figure 15 occurred at two conditions: NPR_{RJ} = 4.0 at H/D_{RJ} = 3 (pressure contour shown in Figure 14b), and NPR_{RJ} = 2.927 at H/D_{RJ} = 6 (Figure 13c). Lastly from Figure 15, there is a significant difference between using only the tap-based integration area and using the entire surface area to calculate the suckdown force. The force at H/D_{RJ} = 2 is approximately 80% of the ideal thrust using the entire area, while the force is calculated to be only 35% of the thrust using the tap-based area. These results combined with Figure 10b suggests that future experiments of this nature will need additional pressure taps to cover the entire underside of the lift plate and to accurately capture the high pressure region due to fountain flow impingement.

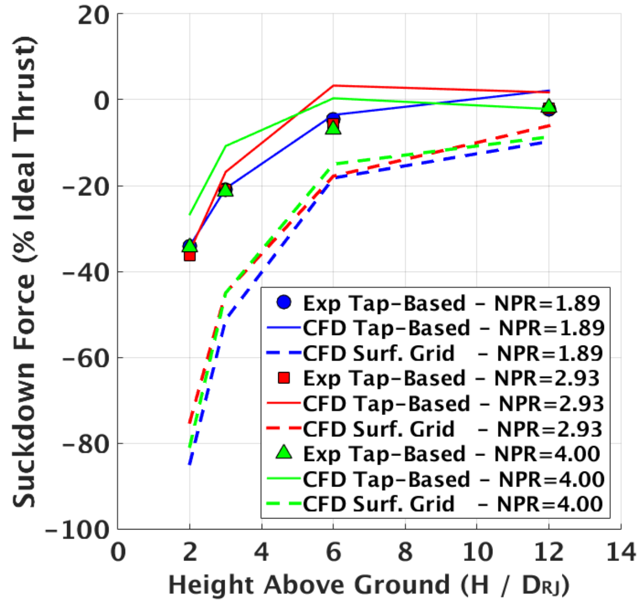

Figure 15. Experimental and CFD suckdown force comparison.

B. Reduced-Order Modeling Results

Several reduced-order models are constructed using the process outlined in Section IIC. A ROM is built individually for each output of interest, including, but not limited to: (1) suckdown force, (2) thrust, (3) mass flow, (4) peak heat flux, (5) peak ground pressure differential, (6) pressure differential at the tap locations on the lift plate, and (7-18) maximum outwash velocity/pressure/temperature at 10, 25, 50, and 100 rear jet diameters from the center of the lift plate. The parameter space selected for the parametric study of these outputs is outlined in Table 2. The included parameters are: (1) height above ground, (2) nozzle pressure ratio of the front sonic jet, (3) total temperature of the front sonic jet, (4) nozzle pressure ratio of the rear supersonic jet, (5) total temperature ratio of the rear supersonic jet, (6) headwind velocity, and (7) ground temperature. The bounds of these parameters are selected based on both the extent of the experimental tests and on engineering judgment in order to discern the impact each parameter has on jet impingement effects.

Table 2. Parameter space and bounds for the ROMs.

Lower Bound	Parameter	Upper Bound
2	Height above ground ($\mathbf{H} / \mathbf{D_{RJ}}$)	24
1.7	Nozzle Pressure Ratio Front Jet ($\mathbf{NPR_{FJ}}$)	2.1
0.95	Total Temperature Ratio Front Jet ($\mathbf{TTR_{FJ}}$)	2.5
1.8	Nozzle Pressure Ratio Rear Jet ($\mathbf{NPR_{RJ}}$)	4.0
0.95	Total Temperature Ratio Rear Jet ($\mathbf{TTR_{RJ}}$)	4.0
0 (m/s)	Headwind Velocity ($\mathbf{U_\infty}$)	15 (m/s)
250 (K)	Ground Temperature ($\mathbf{T_{Ground}}$)	900 (K)

A total of 160 CFD solutions or snapshots are generated by varying the 7 parameters randomly using Latin hypercube sampling from the minimum to maximum values listed in Table 2. Note none of the 160 solutions corresponds to any of the 12 CFD solutions used in the previous experimental comparison. In order to assess the accuracy of the ROMs in a robust manner a repetitive error checking process is employed. First, 10 of the 160 CFD solutions are randomly selected and removed from the database. These solutions represent the *K* snapshots for error evaluation in Figure 5. Next, the ROM is generated by randomly selecting *n* additional snapshots to represent the ROM database. These ROM databases, one for each output of interest, are passed to the DACE toolbox in order to create the kriging interpolation based ROMs. Next, the accuracy of each model is assessed relative to the *K* evaluation snapshots. The whole process from randomly selecting the *K* and *n* snapshots to creating the kriging models and assessing the error is repeated 50 times in order to provide a robust estimate of the error. This process is conducted for values of n ranging from 10 by 10 through 150, in order to give a robust assessment of the accuracy of the ROM relative to the value of n.

Figure 16 shows the average and maximum error for 6 of the ROM outputs considered: (a) suckdown force, (b) total thrust, (c) total mass flow, (d) maximum heat flux at the ground surface, (e) maximum outwash velocity observed at 10 rear jet diameters from the center of the lift plate, and (f) maximum outwash velocity observed at 25 rear jet diameters from the center of the lift plate. The average error is computed as the average of the 10 evaluations averaged over all of the 50 repeats, and the maximum error is the overall maximum observed error in any of evaluations. Also included in this figure is the average and maximum error of a basic linear database interpolation scheme using the same n snapshots as the ROM and comparing to the same K evaluation snapshots. Several clear trends can be observed. First, increasing the number of sample points used to build the ROMs reduces the error, but there are diminishing returns for most of the outputs beyond 100 snapshots. Second, the ROMs outperform linear interpolation for both the average and maximum errors for every output for all numbers of sample points. This demonstrates the advantage that higher order interpolation schemes have over linear interpolation. Finally, using 150 sample points to create the ROMs resulted in average errors less than 10% for every output and maximum errors generally less than 10% for most of the outputs considered. The only ROMs with greater than 10% maximum error were the peak heat flux model, the maximum outwash velocity models, and maximum outwash dynamic pressure models. The ROM with the highest error is shown in Figure 16f, the maximum outwash velocity at 25 rear jet diameters from the center of the lift plate. This output is the most difficult to model due to the highly nonlinear response inside of the parameter space. Finally, note that this model could presumably be improved by including more than 150 snapshots.

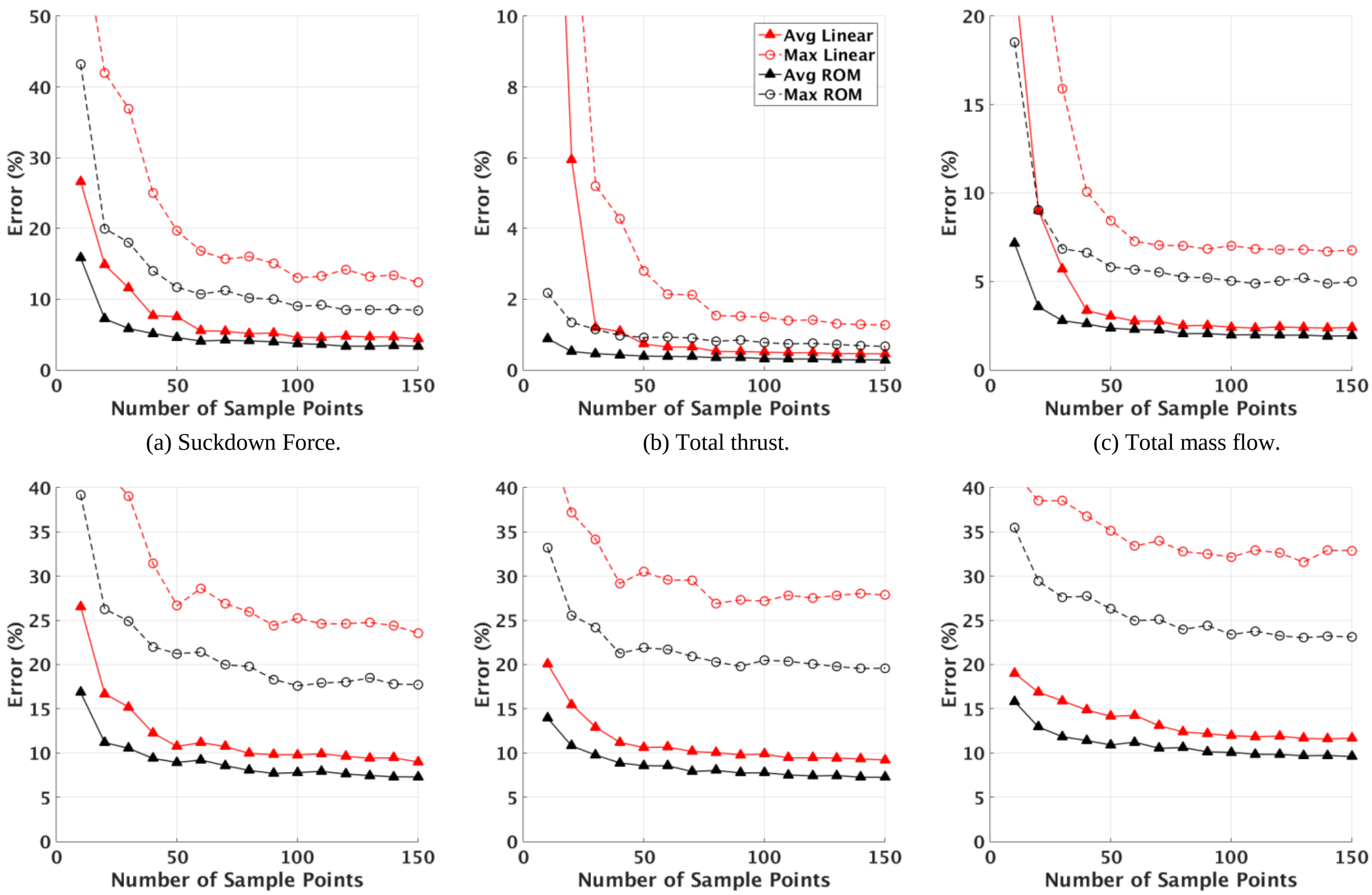

(a) Suckdown Force. (b) Total thrust. (c) Total mass flow.

(d) Maximum heat flux. (e) Maximum outwash velocity @ $10D_{RJ}$. (f) Maximum outwash velocity @ $25D_{RJ}$.

Figure 16: ROM error and linear database interpolation error relative to CFD vs. number of sample points for several outputs.

The next set of ROM results compare the best 150 snapshot ROMs to the CFD results at the 12 experimental conditions discussed in the previous section. Again, the ROM databases do not include these 12 CFD solutions. Note also the ROM is not compared directly to the experimental results only to CFD, since the goal of a ROM is to replicate the full-order CFD results not the experiment. The non-dimensional pressure differential down the center of the lift plate is presented in Figure 17 and the pressure differential contours at NPR_{RJ} = 1.89, 2.927, and 4.0 are presented in Figures 18, 19, and 20, respectively. In order to remain consistent with Figure 11a, Figure 17a includes only two of the four heights above the ground plane.

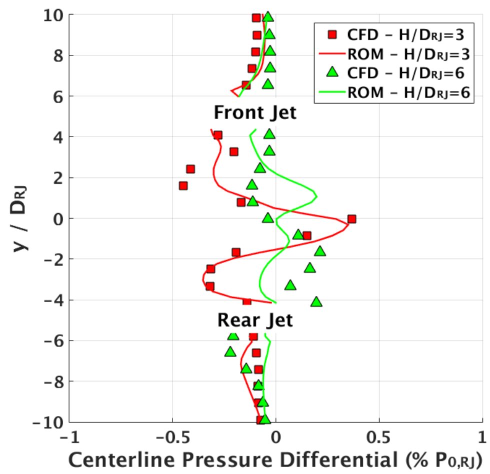

(a) NPR_{RJ} = 1.89.

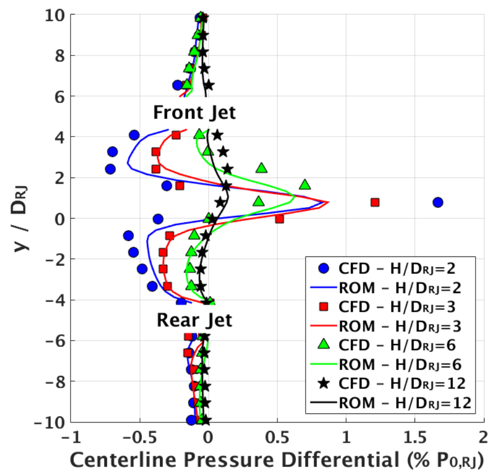

(b) NPR_{RJ} = 2.927.

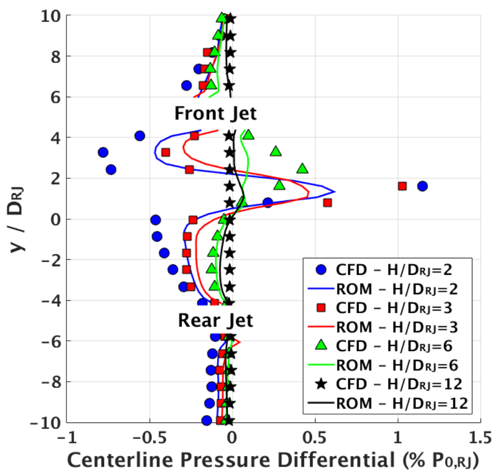

(c) NPR_{RJ} = 4.0.

Figure 17. CFD and ROM non-dimensional pressure differential comparison of the lift plate centerline.

In general, the ROM does a good job of predicting the full-order CFD pressure differentials, as can be seen in Figures 17 through 20. Figure 17 shows that the ROM tends to predict the location of the high pressure region consistently with CFD, however close to the ground the ROM generally under predicts the magnitude. The cases with the worst comparisons are cases in which the ROM is operating near the edge of the parameter space (Table 2); specifically at H/D_{RJ} = 2 for NPR_{RJ} = 1.89 (Fig. 18a) and for NPR_{RJ} = 4.0 (Figs. 17c and 20a). The best comparisons occur right in the middle of the parameter space, specifically NPR_{RJ} = 2.927 (Figs. 17b and 19).

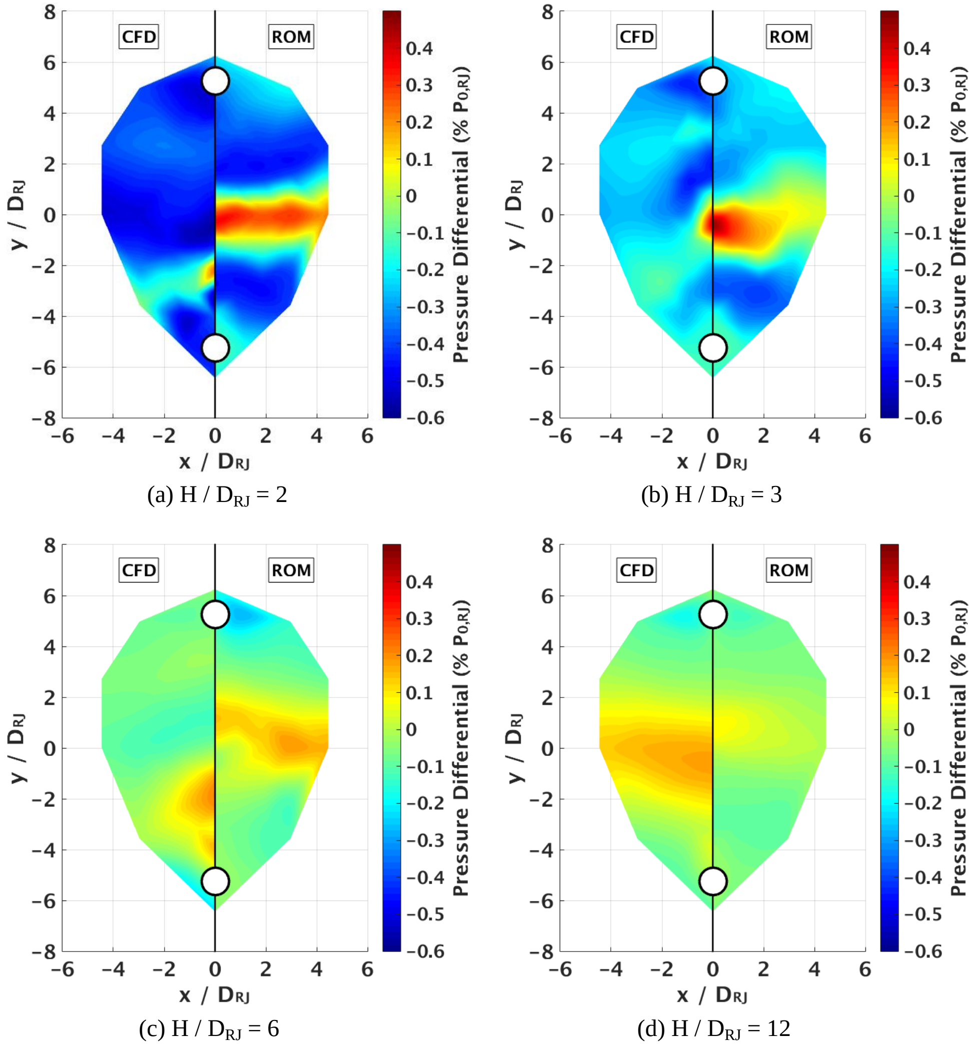

Figure 18. CFD and ROM non-dimensional pressure differential comparisons on the bottom of the lift plate. NPR_{RJ} = 1.89.

ROM and CFD comparisons of the computed suckdown force using the entire bottom surface of the lift plate are provided in Figure 21. Similar trends to those listed for the experimental and CFD comparison (Figure 15) are evident. Additionally, at NPR_{RJ} = 2.927 the ROM and CFD suckdown forces are within 2%, and at the other two nozzle pressure ratios the suckdown forces are within 8%. Note, this ROM is constructed from a database based on the computed suckdown force from 150 snapshots. This ROM does not predict the entire surface pressures and then integrate those pressures into the suckdown force. Thus, the ROM used for the comparison in Figure 21 is different than the ROM in the comparisons used for Figures 17 through 20.

The final study conducted using the ROMs is a parametric sweep of the parameter space. The goal of this sweep is to identify which parameters affect which outputs and to what degree. The parametric sweep is presented in Figure 22 for nine of the outputs: (a) thrust of the rear jet only, (b) mass flow of the rear jet only, (c) suckdown force, (d) peak heat flux magnitude on the ground surface, (e) peak pressure differential on the ground surface, and (f - i) peak outwash velocity at 10, 25, 50, 100 rear jet diameters from the center of the lift plate. These nine outputs represent just a sample of the possible ROM parametric studies.

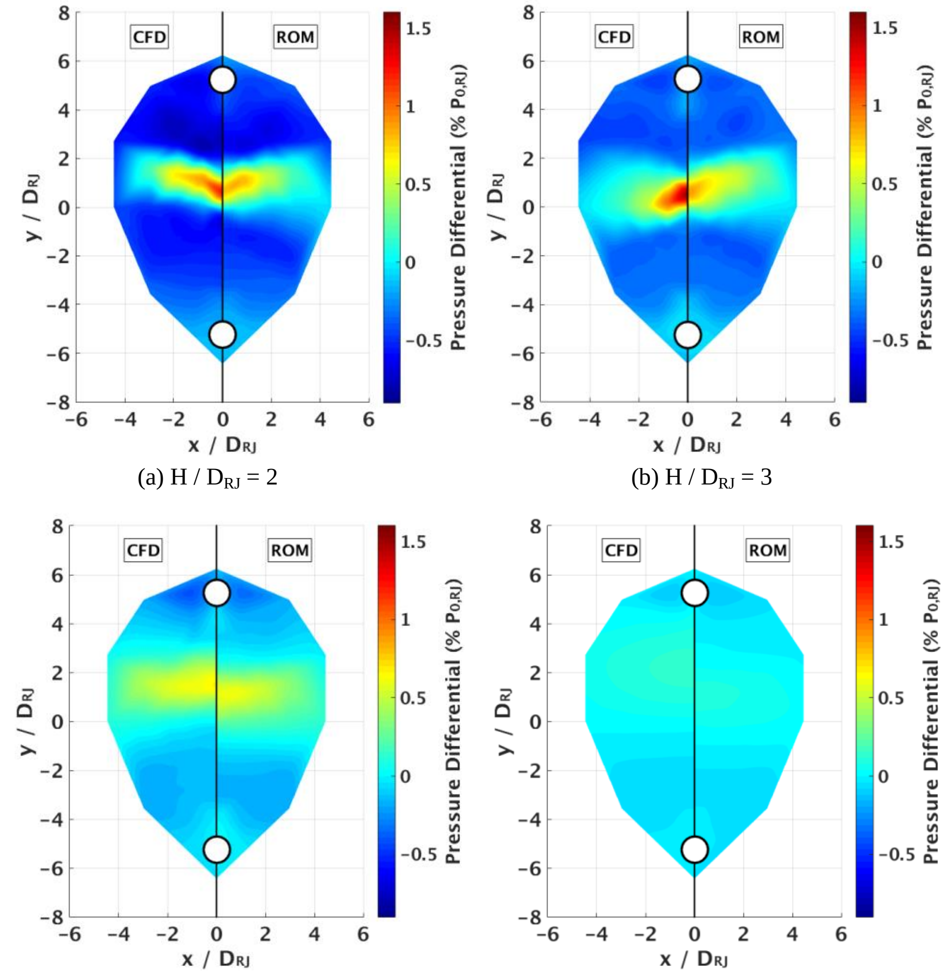

(a) H / D_{RJ} = 2

(b) H / D_{RJ} = 3

(c) H / D_{RJ} = 6

(d) H / D_{RJ} = 12

Figure 19. CFD and ROM non-dimensional pressure differential comparisons on the bottom of the lift plate. NPR_{RJ} = 2.927.

Each of the nine figures inside of Figure 22 are composed of 21 tiles. Each tile is a contour plot based on a 30x30 grid; where one parameter is varied linearly along the x axis and a second parameter is varied linearly along the y axis. The axes are varied from the minimum to the maximum value of each parameter listed in Table 2. Each of the other 5 parameters which are not represented on either the x or y axes of a specific tile are held at the average of the maximum and minimum values of that parameter. The parameters which most impact that response and how they impact the response can be identified by observing where the gradients in the response are the highest. As an example, in Figure 22a, the thrust of the rear jet only changes when NPR_{RJ} is in the x or y axis of a tile. Thus, as expected, the thrust of the rear jet is driven entirely by NPR_{RJ}. In Figure 22b, NPR_{RJ} and TTR_{RJ} drive the mass flow of the rear jet. The height above the ground plane is the dominant parameter for predicting the suckdown force (22c), and plays major roles in the peak ground pressure (22e) and outwash velocities at 10, 25, and 50 rear jet diameters from the center of the lift plate (22f, 22g, and 22h). The peak heat flux (22d) is driven primarily by the ground temperature and TTR_{RJ}, however the height above the ground also plays a role. The freestream velocity parameter only appears to affect the outwash velocities from 25 to 100 diameters away from the lift plate. Note these results are highly dependent on the ranges of the parameters considered. For example, due to the small range of the front jet pressure and temperature ratios listed in Table 2, these parameters play a very little role in any of the outputs considered in Figure 22. However, the front jet parameters do greatly affect the front jet thrust and mass flow, as would be expected. Lastly, unlike previous studies which considered heated jets[2], TTR_{RJ} did not appear to affect the suckdown in this study. Further experimental and computational analysis of this expected but unobserved effect is left for future work.

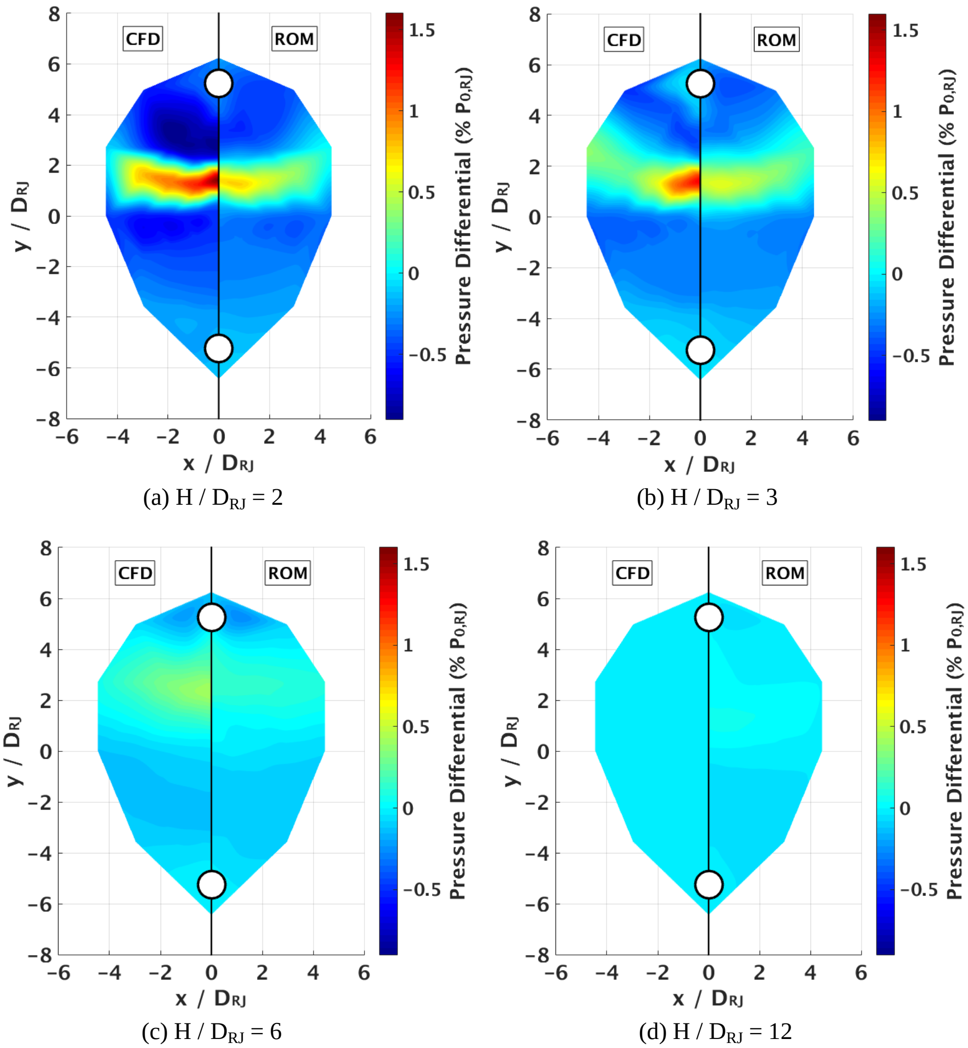

Figure 20. CFD and ROM non-dimensional pressure differential comparisons on the bottom of the lift plate. NPR_{RJ} = 4.0.

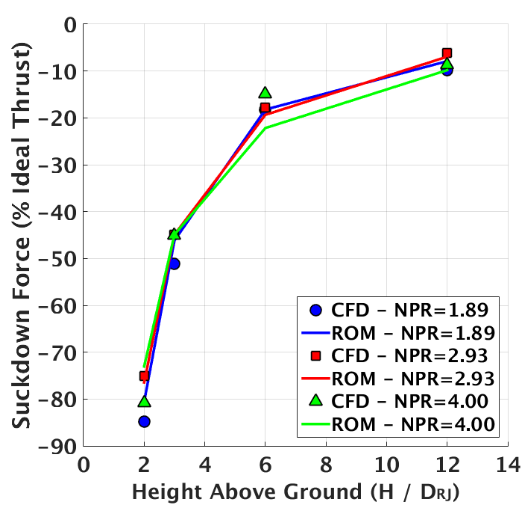

Figure 21. CFD and ROM comparison of the suckdown force over the full lift plate surface.

The last analysis in this study is a computational cost comparison for the parametric sweep. Each of the 21 tiles in one of the blocks in Figure 22 required 900 evaluations. Thus to complete one block requires a total of 18,900 evaluations. An experimental or full-order CFD parametric sweep of this scale would prohibitively expensive. Each CFD solution required on average 10 hours on 512 processors on the AFRL High Performance Computing Center Spirit; a system with over 70,000 2.6GHz Intel Xeon cores. Creating one of the nine blocks in Figure 22, using only full-order CFD solutions, would require over 80 days on 50,000 processors. The ROMs, which do require an initial investment (160 full-order CFD solutions and several minutes to build), on the other hand can generate the 18,900 evaluations for the full parametric sweep in under one second on a single processor.

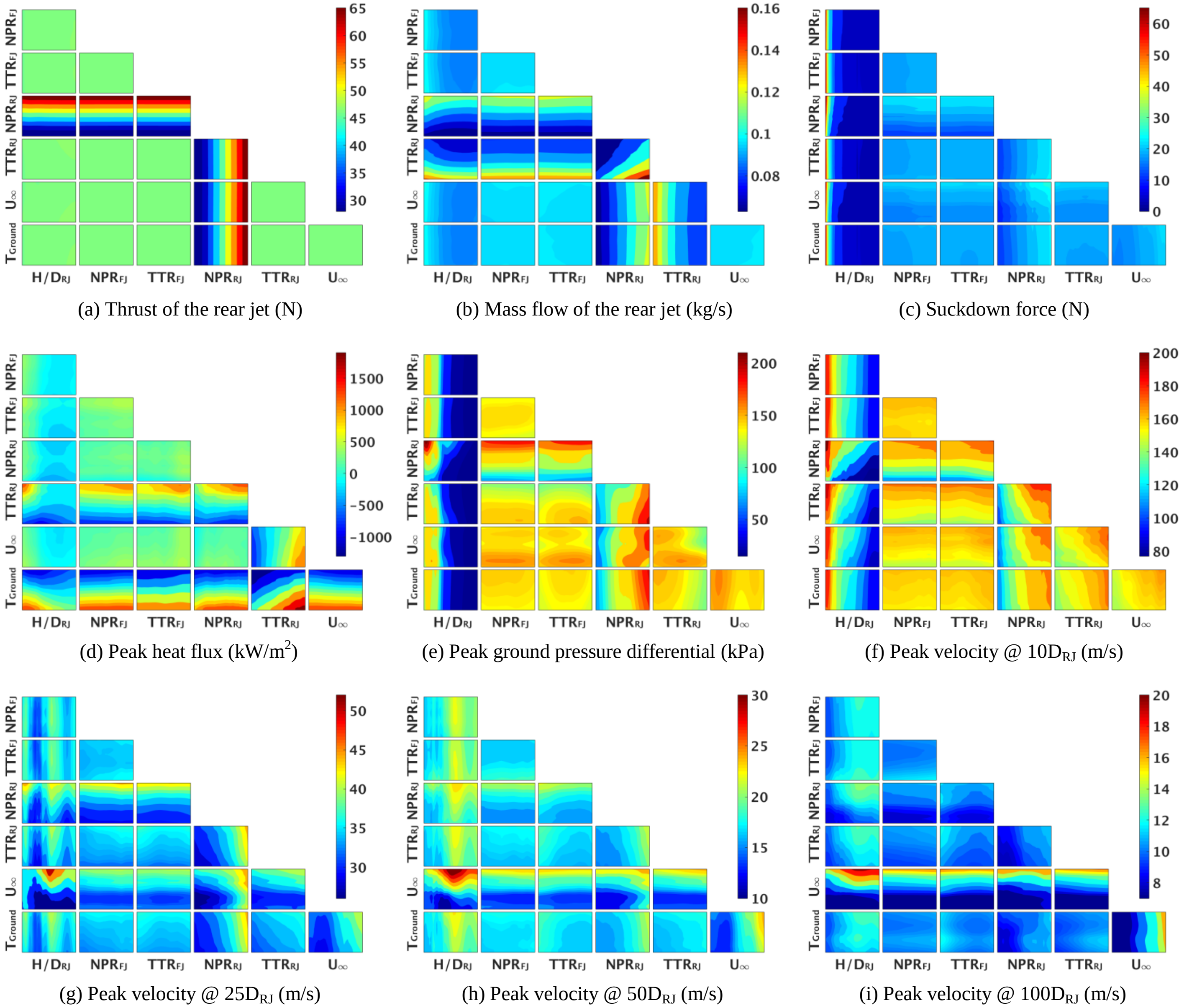

(a) Thrust of the rear jet (N)

(b) Mass flow of the rear jet (kg/s)

(c) Suckdown force (N)

(d) Peak heat flux (kW/m^2)

(e) Peak ground pressure differential (kPa)

(f) Peak velocity @ 10D_{RJ} (m/s)

(g) Peak velocity @ 25D_{RJ} (m/s)

(h) Peak velocity @ 50D_{RJ} (m/s)

(i) Peak velocity @ 100D_{RJ} (m/s)

Figure 22: Parametric sweep using the ROM. Larger gradients in color indicate parameters which have the largest impact on the output of interest.

IV. Conclusions

Two primary studies are conducted, (1) full-order CFD comparison with experiment and (2) a reduced-order model comparison with full-order CFD. In the first study, four turbulence models were assessed relative to experiment for a supersonic nozzle plume. Both the SA and SST turbulence models provided the closest match to the experiment, however there is certainly room for improvements to both of these turbulence models for this application. The SST model was used for the comparison with experiment for the dual jet model in ground effect. Comparisons were made for the pressure differential observed on the underside of the lift plate for three different rear jet nozzle pressure ratios and four different lift plate heights above the ground. Several general conclusions can be drawn from this study: first, the CFD model generally predicted the correct location of the high pressure region due to the fountain flow impingement. Second, at the positions closest to the ground considered in this study the CFD model over predicted the strength of the high pressure region. Third, the computed suckdown force based on the tap locations compared reasonably well between CFD and the experiment. However, based on the CFD results, the tap locations do not adequately capture the pressure distribution on the bottom of the lift plate; the high pressure region can be easily missed due to the spacing of the pressure taps. Additionally, up to 45% of the suckdown force is not accounted for inside of the area covered by the tap locations. Specifically, the CFD model showed the suckdown force as high as 80% of the ideal thrust using the entire surface, but the tap based integration only resulted in a suckdown force of 35% of the ideal thrust. Finally, this study showed similar results to previous studies, such as the suckdown force increasing dramatically as the lift plate approaches the ground.

In the second part of this study, several ROMs were created, evaluated, and exercised in a large scale parametric sweep. A number of ROMs were created from 160 CFD solutions and every one had less than 10% average error, and most had much lower error. The ROMs were also used to replicate the experimental study. In general, the ROMs accurately predicted the full-order CFD results for these cases, except for the cases near the edge of the parameter space from which the ROMs were created. Finally, the ROMs were used to conduct a large scale parametric sweep in order to identify how each parameter affects each output. One effect that was expected due to previous studies using single jets[2] but was not observed in this study was an increase in the suckdown force due to an increase in the total temperature. This result may warrant further experimental and computational analysis. Lastly, a computational cost comparison between CFD and the ROMs was conducted. After the initial investment to build the ROMs, the computational cost to produce the parametric sweep was one second on one processor; while an equivalent study using full-order CFD would have required over two and a half months to complete on 50,000 processors.

V. Acknowledgements

The experimental portion of this work was performed using funds from a DURIP grant under the sponsorship of the Office of Naval Research; Dr. Brenda Henderson serving as Project Monitor. The active participation of Prof. Dennis McLaughlin, Prof. Philip Morris, Mr. Russell Powers and Mr. Nicholas Rudenko in the planning and conducting of the laboratory experiments is gratefully acknowledged. The second author was supported by a DoD SMART Scholarship affiliated with the Naval Air Warfare Center – Aircraft Division, Patuxent River, with Dr. David Findlay serving as mentor. Additionally, this work was partially funded through the ILIR Program at the Naval Air Warfare Center – Aircraft Division, Patuxent River, with Dr. James Sheehy and Mr. Jerry Rubinsky serving as Project Monitors.

References

[1] Krothapalli, A., Rajkuperan, E., Alvi, F.S., and Lourenco, L., "Flow field and noise characteristics of a supersonic impinging jet," *Journal. of Fluid Mechanics*, Vol. 392, pp. 155-181, 1999.

[2] Kumar, R., Lazic, S., and Alvi, F.S., "Control of high-temperature supersonic impinging jets using microjets," *AIAA Journal*, Vol. 47, No. 12, 2009, pp. 2800-2811.

[3] Curtis, P., "A review of the status of ground effect/environment technologies," AIAA 2002-5985, 2002.

[4] Alvi, F.S., Ladd, J.A., and Bower, W.W., "Experimental and Computational Investigation of Supersonic Impinging Jets," *AIAA Journal*, Vol. 40, No. 4, 2002, pp. 599-609.

[5] Fluk, H., "Runway and deck temperatures in vertical takeoff/landing operations," *AIAA Aircraft Systems and Technology Conference*, AIAA Paper No. 81-1623, 1981.

[6] Silva, M. J. and Riser, R., "CH-47D tandem rotor outwash survey," AHS 67th Annual Forum, 2011.

[7] Leishman, J. G., *Principles of helicopter aerodynamics*, Cambridge University Press, 2007.
[8] McCarthy, K., "The JSF STOVL performance process from small-scale database to flight test demonstration," AIAA 2002-6002, 2002.
[9] Platzer, M.F., and Margason, R.J., "Prediction Methods for Jet V/STOL Propolsion Aerodynamics", *Journal of Aircraft*, Vol. 15, No. 2, 1978, pp. 69-77.
[10] Krothapalli, A., Choutapalli, I., Alkislar, M., and Lourenco, L., "Accoustics of twin supersonic impinging jets", *9th AIAA/CEAS Aeroacoustics Conference and Exhibit*, AIAA Paper No. 2003-3316.
[11] Saddington, A.J., Knowles, K., and Cabrita, P.M., "Flow Measurements in short takeoff, vertical landing fountain: splayed jets", *Journal of Aircraft*, Vol. 46, No. 3, 2009, pp. 874-882.
[12] Myers, L.M., and McLaughlin, D.K., "Outwash Measurements of a dual impinging jet scale model", *53rd AIAA Aerospace Sciences Meeting*, AIAA Paper No. 2015-1937.
[13] Li, Q., Page, G.J., and McGuirk, J.J., "Large-eddy simulation of twin impinging jets in cross-flow", *The Aeronautical Journal*, Paper No. 3097, 2007.
[14] Erwin, J.P., Sinha, N., and Rodebaugh, G.P., "Large eddy simulations of supersonic impinging jets", *Proceedings of ASME Turbo Expo*, 2012, Paper No. GT2012-70140.
[15] Dewan, Y., Golubev, V.V., Lyrintzis, A.S., Mankbadi, R.R., Kurbatskii, K.A., and Osman, E., "Detached eddy simulations of supersonic jets impinging on flat plates", *43rd Fluid Dynamics Conference*, 2013, AIAA Paper No. 2013-3097.
[16] Brown, M.R., and Frendi, A., "Supersonic jet impingment on a flat plate", *18th AIAA/CEAS Aeroacoustics Conference*, 2012, AIAA Paper No. 2012-2261.
[17] Crowell, A.R. and McNamara, J.J., "Model Reduction of Computational Aerothermodynamics for Hypersonic Aerothermoelasticity," AIAA Journal, Vol. 50, No. 1, January 2012, pp. 74-84.
[18] Myers, L.M., "Investigation of the Flow-Field of Two Parallel Round Jets Impinging Normal to a Flat Surface", Ph.D. Dissertation, Aerospace Engineering, The Pennsylvania State University, 2015.
[19] Strang, W., Tomaro, R., and Grismer, M., "The Defining Methods of Cobalt: A Parallel, Implicit, Unstructured Euler/Navier-Stokes Flow Solver", AIAA Paper 99-0786, Jan. 1999.
[20] Spalart, P.R., and Allmaras, S.R., "A One-Equation Turbulence Models for Aerodynamic Flows," *La Recherche Aerospatiale*, Vol 1, June 1994, pp. 5-21.
[21] Menter, F.R., and Rumsey, C.L., "Assessment of Two-Equation Turbulence Models for Transonic Flows," AIAA Paper 1994-2343, June 1994.
[22] Spalart, P.R., "Detached-eddy simulation," *Annual Review of Fluid Mechanics*, Vol. 41, 2009, pp. 181-202.
[23] Menter, F.R., and Kuntz, M., "Adaptation of eddy-viscosity turbulence models to unsteady separated flow behind vehicles." *The aerodynamics of heavy vehicles: trucks, buses, and trains*. Springer Berlin Heidelberg, 2004, pp. 339-352.
[24] Pirzadeh, S., "Three-Dimensional Unstructured Viscous Grids by the Advancing Front Method," *AIAA Journal*, Vol. 34, No. 1, Jan. 1996, pp. 43-49.
[25] Marcum, D.L., and Weatherill, N.P., "Unstructured Grid Generation Using Iterative Point Insertion and Local Reconnection," *AIAA Journal*, Vol. 33, Sept. 1995, pp. 1619-1625.
[26] Lophaven, S.N., Nielsen, H.B., and Sondergaard, J., "DACE A Matlab Kriging Toolbox Version 2.0," TR-IMM-TR-2002-12, Aug. 2002.
[27] Queipo, N.V., Haftka, R.T., Shyy,W., Goel, T., Vaidyanathan, R., and Tucker, P.K., "Surrogate-Based Analysis and Optimization," *Progress in Aerospace Sciences*, Vol. 41, January 2005, pp. 1–28.